-

Analysis of Nonlinear Decoherence in the IOTA Ring

C. C. Hall
RadiaSoft LLC
(Dated: November 30, 2018)

The Integrable Optics Test Accelerator (IOTA) has been built at Fermi National Laboratory for study of nonlinear integrable optics. The use of nonlinear integrable optics shows great promise in providing control of deleterious coherent effects through use of a special nonlinear magnetic element that will provide large tune spread with amplitude while still constraining the idealized dynamics by two invariants. In this work we examine what happens when the idealized design principles required by this nonlinear element for the rest of the lattice are broken due to space charge. It is observed that while the two invariants are no longer maintained there is still suppression of coherent effects. The scaling of the nonlinear decoherence is examined through simulation studies in the case of space charge and an analytic model is provided for the case of vanishing space charge.

I. INTRODUCTION

Modern hadron accelerators such as spallation sources and neutrino factories must reach higher beam intensities to meet increasingly challenging demands on performance. For example, the European Spallation Source plans for a proton beam with $5\,\mathrm{MW}$ average power [1]. The Proton Improvement Plan (PIP) at Fermilab [2], intended to drive neutrino experiments, will top $1\,\mathrm{MW}$ with the ability to expand beyond that for future upgrades. To maintain an acceptable beam loss of $1\,\mathrm{W/m}$, fractional losses must be kept very low, with PIP-II requiring losses beneath 0.3% and future designs requiring many times less.

As beam power increases, its stability and lifetime may be compromised by coherent collective effects due to direct space charge – the canonical example of this is beam halo [3–6]. Other effects that can lead to beam loss in storage rings include dipole wake instabilities [7, 8] where the growth rate is proportional to the beam current; the transverse microwave instability [9] which has a threshold intensity; and the head-tail instability [10] which does not.

Each of these instabilities arise in part due to strong linear focusing driving betatron resonances at a single frequency. Head oscillations at this frequency resonantly drive the tail of the bunch in wake field driven instabilities, while transverse envelope oscillations at twice the betatron frequency in the presence of space charge produce beam halo. Introducing tune spread with amplitude can suppress these resonant interactions. If there is a transverse tune spread ΔQ, any transverse oscillations will decohere in a time $\tau \sim \Delta Q^{-1}$. For decoherence times smaller than the growth rates of the instabilities, the driving terms will damp before any beam instability can grow.

One proposed tool to mitigate these coherent instabilities is the nonlinear integrable optics [11, 12], which introduce large transverse tune spreads while still maintaining bounded, regular orbits. The principle is to construct an accelerator lattice which leads to bounded, regular motion in the transverse plane for on-momentum particles with large tune spreads. The large tune spread damps any oscillations which would normally drive coherent space charge instabilities [13]. The Integrable Optics Test Accelerator (IOTA) is being commissioned at Fermi National Laboratory for study of the concept of nonlinear integrable optics [14]. The use of a special nonlinear magnetic element introduces large tune spread with amplitude while constraining the idealized dynamics by two integrals of motion. However, integrability is susceptible to perturbations in the presence of space-charge, including tune-shift and transverse beam mismatch.

We present simulations of the IOTA ring demonstrating the viability of the nonlinear integrable optics in the presence of space charge. We first illustrate the proper procedure for creating a matched beam for the nonlinear system. We then present a lattice design scheme that corrects for perturbations arising from space-charge driven tune shift that would otherwise disrupt integrability. The efficacy of this scheme is them demonstrated by examining nonlinear decoherence, produced by the elliptic element, in the case of an offset injected bunch. Finally, an analytic model is provided to examine some of the scaling observed from simulations in the previous sections.

II. CREATING A MATCHED BUNCH

For a periodic accelerator matching of the bunch to the lattice usually entails finding a periodically constant set of Twiss parameters. The statistical properties of the distribution are then set equal to the Twiss parameters of the lattice. Thus matched such a bunch will remain stable in time.

For matching of a bunch to a lattice including an elliptic nonlinear element we use two versions of the lattice. The first is the base lattice without any nonlinear elements, using this lattice we can obtain the matched Twiss parameters that will be needed to construct the bunch. For the actual construction of the bunch we make use of the nonlinear potential that will be created based on the

parameters of the nonlinear element. It has been found that such a matching procedure is necessary to prevent beam loss [15].

For an idealized Kapchinskij-Vladimirskij (KV) distribution all particles will have an identical value for the Hamiltonian

$$H = \frac{\hat{p}_x^2}{2} + \frac{\hat{p}_y^2}{2} + \frac{\hat{x}^2}{2} + \frac{\hat{y}^2}{2} + tU(\hat{x}, \hat{y}). \qquad (1)$$

So that all particles lie on a single hyper-ellipsoid in the transverse phase space. While the KV distribution is useful due to its linear space charge forces which means that all particles experience a single tune depression it is also prone to producing numerical effects and has been found to not produce long-term stable results in simulation.

For this reason we use a waterbag distribution is used in these studies. We define a waterbag to be

$$f(H) = \begin{cases} 1 & H_{max} - H > 0 \\ 0 & H_{max} - H < 0 \end{cases}, \qquad (2)$$

where H, the Hamiltonian is defined in Eq. 1 and H_{max} is a chosen cutoff value. The bunch is populated by generating trial particles inside the real space coordinates bounds of the chosen equipotential cutoff H_{max}, if the particle has $tU \leq \varepsilon$, where ε is the usual emittance, then the momentum coordinates of the particle are assigned based on the quantity $\varepsilon - tU$. An example of the resulting distribution is shown in Fig. 1.

III. SIMULATIONS OF IOTA

A. Simulation Descriptions

Simulations of IOTA were performed with the tracking code Synergia [16]. Space charge forces were calculated using a self-consistent 2.5D model that slices the beam longitudinally and then applies transverse kicks to the bunch calculated for each slice. As we are primarily concerned with transverse effects a very long bunch $\sigma_z \gg \sigma_{x,y}$ was used with zero initial momentum spread. Under these conditions the space charge kick should be almost entirely uniform along the bunch reducing the space charge model to 2D.

The lattice elements are all modeled using first-order maps to prevent mismatch produced from higher-order effect creating a loss of integrability beyond that which will be produced by space charge. The exception to this is the nonlinear magnet which is modeled using a second order drift kick approach. The elliptic potential is a function of a strength parameter t and geometric parameter c. For invariance to be maintained these parameters must scale with the β-function as β^{-1} and $\sqrt{\beta}$ respectively along the nonlinear magnet. For construction of
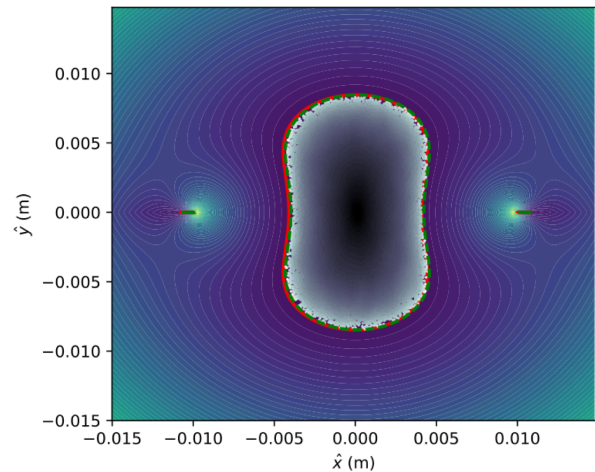

FIG. 1: A waterbag distribution is shown in normalized coordinates, superimposed over the elliptic potential. Equipotential lines are shown in grey with the maximum equipotential for the bunch outlined in red and shifted equipotential marked in green.

the physical magnet smooth scaling is not realistically achievable due to engineering constraints and the magnet is broken into 20 thin slices [17]. In simulation, it has been seen that 20 slices with the second order drift-kick scheme is sufficient to provide convergence. In our simulations with the inclusion of space charge we use 60 slices to ensure good convergence.

B. Adaptive matching for space charge compensation

Integrability is crucially dependent upon the $n\pi$ phase advance condition between nonlinear segments. We derived a lattice adjustment procedure to retain this condition across varying beam distributions and currents. First, a new working point for the linear lattice must be constructed to preempt the space charge tune shift, ΔQ. Simulations performed with sixdsimulation were used to adjust quadrupole strengths in order to offset the phase advance between the exit and entrance by the desired amount for a range of ΔQ values [18].

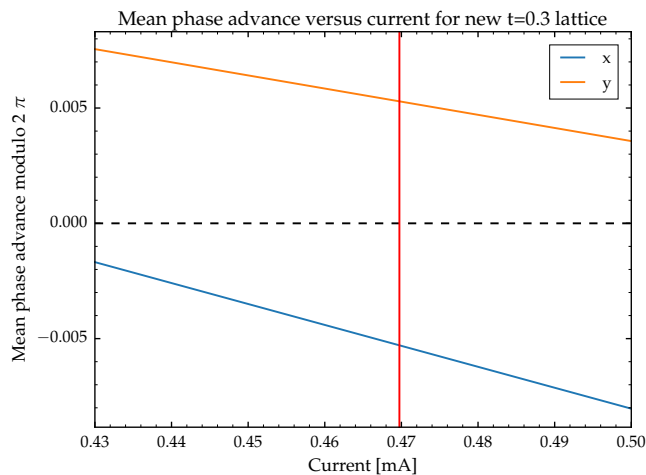With the linear lattice adjusted, we then sought a

FIG. 2: The operating current for an adjusted IOTA lattice is found by minimizing the deviation in the phase advance in each plane from zero.

FIG. 3: Centroid (C_x) motion for a matched bunch displaced horizontally by $100\,\mu$m. Motion with the nonlinear element off is shown in blue and with nonlinear element on in orange. Space charge is not included in the simulation.

TABLE I: Characteristics of the bunch and lattice for simulations.

Quantity	Value	Units
Beam Parameters		
dQ_{SC}	0.03	-
ε_0	4, 8, 12, 16	$mm - mrad$
I	0.2056, 0.4113, 0.6169, 0.8225	mA
K	2.5	MeV
Δx	100	μm
Nonlinear Magnet Parameters		
t	0.2/0.4	-
c	0.01	$m^{1/2}$
ψ_{nll}	0.3	2π

beam current that provided the appropriate tune depression for the full nonlinear lattice. Because the nonlinear potential is asymmetrical, the tune shift varies in each plane as a function of the nonlinear strength t, and thus requires a nontrivial adjustment to the beam current for each configuration. To determine the operating current for a lattice, a single turn was simulated in Synergia using its explicitly linear space charge solver. Particle coordinates were sampled at the exit and entrance of the nonlinear element. Small amplitude particles were chosen such that an accurate linear normal form could be computed. A linear phase unwrap algorithm was then applied to the particles normalized coordinates and a mean phase advance in each plane was computed for the input beam current. The resulting distribution of phase advances in both planes is illustrated in Fig. 2. The optimum current is indicated by the value for which ϕ_x and ϕ_y are equally close to zero.

This procedure was repeated to construct optimized lattice and beam configurations for each combination of tune-depression and t value considered.

C. Simulation Results

To examine the operation of the nonlinear element we start the simulation with a bunch that has been matched into the elliptic potential as previous described, but after the matching procedure the bunch centroid is displaced from zero in x by $100\,\mu$m. A comparison of bunch centroid motion with and without the nonlinear element is shown in Fig. 3 With a purely linear lattice this displaced bunch exhibits coherent oscillations of the centroid around zero indefinitely. With the nonlinear element turned on these oscillations rapidly damp due to the tune spread created by the nonlinear magnet. Be-
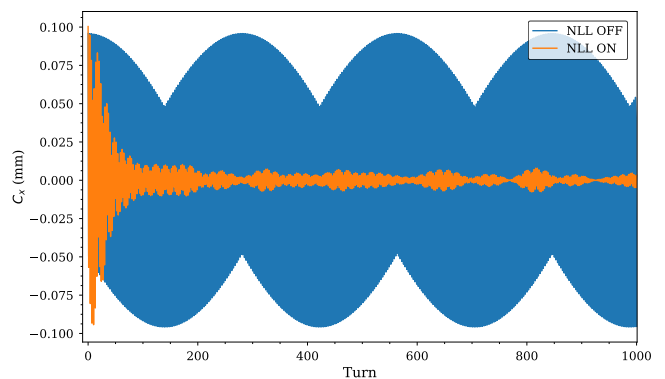
cause the multipole expansion of the elliptic potential has a quadrupole term in the lowest order there is a splitting of the horizontal and vertical tunes, as well as the spread from the higher-order terms.

1. Nonlinear Decoherence with Space Charge

We now illustrate what happens when space charge is included in the simulation. The space charge model used in Synergia was previously discussed. For all simulations with space charge a tune depression of $0.03 \times 2\pi$ / turn is maintained. For a waterbag bunch distribution an asymmetric distribution of tunes, shifted from the lattice design point, occurs. To match the beam current to the ideal tune depression as closely as possible a scan over the current is performed. The ideal current is selected to that which maximizes the number of particles in the bunch that have a phase advance from the exit to the entrance of the nonlinear element within one standard deviation of zero. Values for various emittances are shown in Table. I.
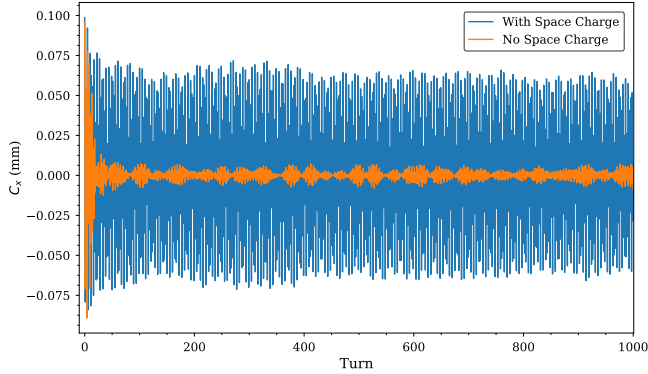
FIG. 4: Centroid (C_x) motion for a matched bunch displaced horizontally by $100\,\mu\text{m}$. Only single particle dynamics are considered for the simulation in orange. Space charge is included for the simulation shown in blue.

FIG. 5: Centroid (C_x) versus turn number for bunches of varying emittance propagated in IOTA for $10\,000\,\text{turns}$. The inset shows the first $10\,000\,\text{turns}$ magnified.

For a bunch with an initial emittance of $8\,\text{mm} - \text{mrad}$ and with a nonlinear magnet strength $t = 0.4$ the turn-to-turn centroid motion is shown in Fig. 4. It is seen that with space charge now included the damping time is greatly increased and one thousand turns is no longer sufficient to see the centroid motion decrease appreciably. The main culprit for this loss in effectiveness of nonlinear decoherence is the space charge induced tune spread. The assumption of time-invariance created by the ideal T-insert is broken for particles that do not maintain the design tune.

IV.   EMITTANCE SCALING OF NONLINEAR DECOHERENCE

The presence of even a relatively modest amount of space charge, as measured from the average tune depression created can have significant impact on the behavior of the nonlinear decoherence. In this section we will examine the behavior of nonlinear decoherence over a longer time scale and with varying emittance of the waterbag distribution. The parameters of Table. I remain relevant in this section for the appropriate emittance value.

Using the matching procedure described in Section. II a matched bunch is created and the space charge tune depression is adjusted to match the nominal value of $dQ_{SC} = 0.03$ as closely as possible. The means that each different emittance value will have a different average current. These bunches are started at the center of the nonlinear element in IOTA, each with an offset of $\Delta\sigma_x = 100\mu m$. The simulations are run for $10\,000\,\text{turns}$ and the bunch phase space recorded at center of the nonlinear element ever four turns.

The results for each simulation from $4\,\mu\text{m}$ to $16\,\mu\text{m}$ is shown in Fig. 5. It is apparent that the damping rate of the centroid motion from the nonlinear decoherence is strong dependent on bunch emittance. The scale ranges
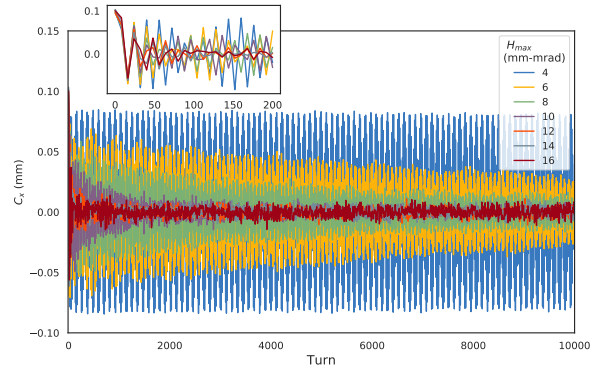
from $>10^5$ turns for small emittance down to $<200\,\text{turns}$ for the upper emittance range. There is also a change in behavior of the centroid motion exhibited from the first few turns, where there is a very rapid change from the initial offset, to an intermediate regime that may be described, approximately, as an exponential decay of the centroid versus turn envelope. Finally, there is some floor reached for the centroid oscillations, independent of the emittance.

The corresponding invariants are shown in Fig. 6. The first invariant, H, corresponds to the Hamiltonian, as given in Eq. 1 with the elliptic potential U, and is directly related to the emittance. The second invariant I is described in [11]. There is a long-term linear growth in invariants for all emittances. However, it is clear that while the invariants are not exactly preserved there is still significant preservation of the beam against coherent effects, as demonstrated by the centroid oscillation damping.

To estimate the the dependence of nonlinear decoherence on emittance we can use an exponential decay $C(T) = C_0 e^{-T/\tau}$ to fit to the centroid oscillation damping. This fit begins on turn 5, to allow for the initial, more rapid, decay period and is based on the normalized absolute value of the centroid position by turn. The resulting fit with each centroid dataset is show in Fig. 7. For fits of larger emittances the fit naturally tends to follow the early falloff due to how heavily it is weighted compared to the very-long, low-amplitude tails.

The resulting decay rates, τ, are summarized in Fig. 8. While a roughly exponential dependence on emittance is shown up until $12\,\text{mm} - \text{mrad}$ the trend falls off for the higher emittances. This may be a result of the extremely rapid damping on the overall time scale of the entire simulation.
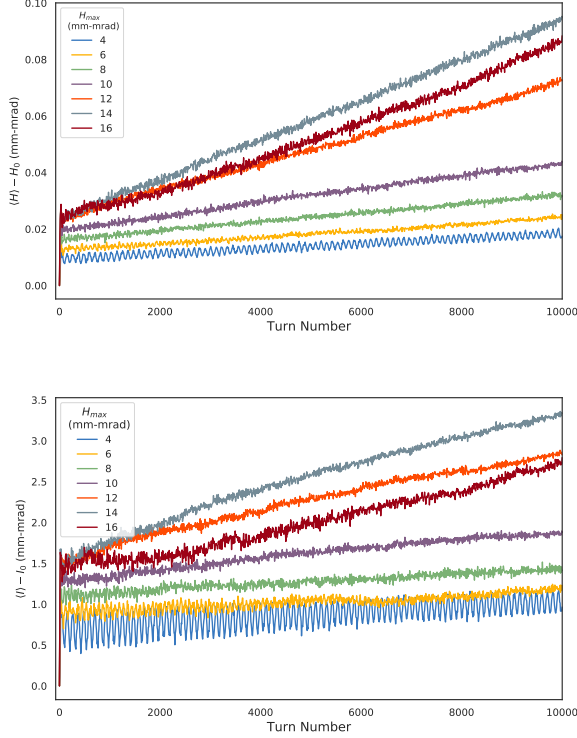
FIG. 6: First and second invariants (on top and bottom figures respectively) versus turn number.

V. 1D ANALYTIC DECOHERENCE MODEL

We now move to describing a basic model for the centroid motion of bunch undergoing nonlinear decoherence. To begin we assume that the bunch starts out with some displacement Δx along one transverse axis at turn $N = 0$. We will then find a representation of $\hat{x}(N)$ the normalized centroid position $\langle x \rangle / \sigma_x$ as a function of turn number.

The method for describing the centroid behavior of a gaussian distribution was originally given by Meller et al. [19] and describe particle motion in the coordinates $a = \sqrt{\beta_x \varepsilon_x} / \sigma_x$ and φ, for the amplitude and initial phase of a particle. This means that the actual particle displacement is then $x = \sigma_x a \cos(2\pi\nu N + \varphi)$.

Because of the presence of the nonlinear element there will be amplitude-dependence in the particle tune. may be characterized in terms of a unitless strength parameter t and geometric scale factor c, with units of $m^{\frac{1}{2}}$, that describes the location of two singularities in the x-plane. The first few terms of the multipole expansion for the elliptic potential in normalized coordinates $\hat{x}, \hat{y} = x/\sqrt{\beta}, y/\sqrt{\beta}$ are given by

$$U(\hat{x}, \hat{y}) = \frac{-t}{c^2} \, Im \left\{ (\hat{x} + i\hat{y})^2 + \frac{2}{3c^2}(\hat{x} + i\hat{y})^4 + \right.$$
$$\left. \frac{8}{15c^4}(\hat{x} + i\hat{y})^6 + ... \right\}. \quad (3)$$

Note: this expansion is only valid in the region $\sqrt{\hat{x}^2 + \hat{y}^2} < c$. Because of the form of the potential we expect to see just the even terms in amplitude effecting the tune.

A. Nonlinear Decoherence and the Centroid

Due to the octupole and higher terms in the potential the tune ν will have an amplitude dependence of the form

$$\nu = \nu_0 - \sum_{i=1} \mu_i a^{2i}, \quad (4)$$

where ν_0 is the unperturbed tune and μ_i are coefficients determined by the octupole, duodecapole, etc. multipole components in the nonlinear element. The calculation of these coefficients becomes cumbersome beyond the lowest order. This is a major obstacle to the use of the formulation developed here. This issue will be discussed further on.

This amplitude-dependent tune will result in particles having a phase shift each turn of

$$\Delta\varphi(a, N) = -2\pi N \sum_{i=1} \mu_i a^{2i}, \quad (5)$$

when compared to the unperturbed phase advance ν_0. From this the centroid motion for a distribution $\rho(a, \varphi)$ as a function of turn number in a lattice with some nonlinearities will be

$$\hat{x}(N) = \int_0^\infty da \int_0^{2\pi} d\varphi \, a\cos(\varphi)\rho(a, \varphi - 2\pi N\nu). \quad (6)$$

B. Calculation for a Waterbag Distribution

Because all our simulation data we will compare to uses a waterbag distribution we are first interested in the calculation of Eq. 6 for such a distribution. here we define a 'waterbag' according to the definition of Reiser, that is the bunch has a uniform distribution of particle amplitudes from 0 to some cutoff, that is

$$\rho(a, \varphi) = \begin{cases} 1 & a \leq 1 \\ 0 & a > 1 \end{cases} \quad (7)$$

.

We then assume that the distribution starts out with a centroid offset, in our normalized coordinates is, $Z = \Delta x / \sigma_x$. This offset waterbag then takes form

$$\rho(a, \varphi) = \begin{cases} \frac{1 + Z^2 - 2Z\cos(\varphi)}{\pi} & 0 < a \leq 1 \\ 0 & a > 1 \ o \ ra < 0 \end{cases} \quad (8)$$
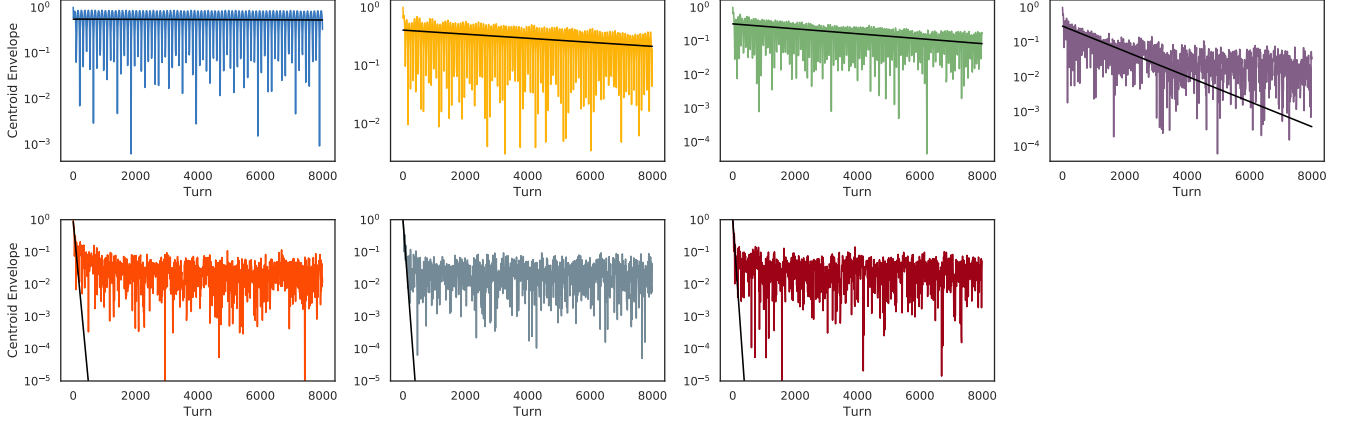
FIG. 7: Fit of exponential decay for $|C_x|/C_x^{(0)}$ shown in black for each emittance in their respective color each on a semi-log scale.
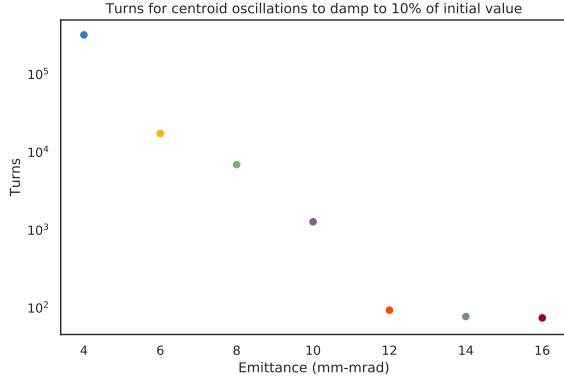

FIG. 8: Decay rate τ versus emittance shown on a semi-log scale. Color coded by emittance.

Inserting Eq. 8 in Eq. 6 we can make a convenient change of variable $u = a^2$ and perform the integration in φ, resulting in

$$\hat{x}(N) = \pi Z \int_0^1 du \, \cos(2\pi\nu_0 N)\cos(\Delta\varphi(u,N))+$$
$$\sin(2\pi\nu_0 N)\sin(\Delta\varphi(u,N)) \quad (9)$$

A second change of variable $\hat{u} = 2\pi N u$ is then made to assist in numerical integration down the road. The general result for the centroid motion is then

$$\hat{x}(N) = \frac{Z}{2N} \int_0^{2\pi N} d\hat{u} \, \cos(2\pi\nu_0 N)\cos(\Delta\varphi(u,N))-$$
$$\sin(2\varphi\nu_0 N)\sin(\Delta\varphi(u,N)) \quad (10)$$

After this transformation the phase slip $\Delta\varphi$ has now become

$$\Delta\varphi(\hat{u},N) = \sum_{i=1} \frac{\mu_i \hat{u}^i}{(2\pi N)^{i-1}}. \quad (11)$$

C. Comparison to Simulations

For the case where only the quadratic amplitude term is used the expected coupling strength may be estimated from [20]

$$\mu_1 = \frac{3\varepsilon}{16} \sum_{i=1}^n k_{3,i}\beta_{x,i}^2, \quad (12)$$

where the octupole strength of a segmented representation of the nonlinear element of length l is

$$k_{3,i} = \frac{16}{n} \frac{t\ell}{c^2\beta_{x,i}^3}. \quad (13)$$

In the ideal case the field in the magnet should continuously and smoothly vary along the length of the element. In the actual nonlinear element the the magnet is composed of 20 segments to approximate this variation. In our simulation the magnet is split into 60 segments for slightly better convergence. The matched betatron function calculated for the element and the resulting variation in k_3 are shown in Fig. 9.

For comparison to this model bunches with several different emittances were again simulated in IOTA using Synergia. In each cases the bunch was started with an offset of 100 μm in the x centroid. The nonlinear element used the same parameters from Table I. It should be noted that the model of the nonlinear element with the full elliptic potential (that is, no truncated multipole expansion) was used in the simulations, as compared to the analytic model with only an octupole term.
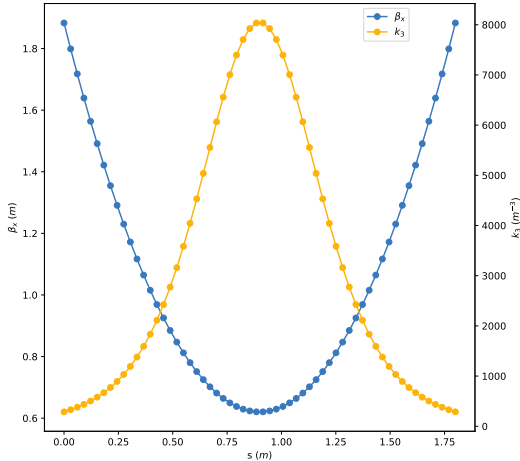
FIG. 9: The betatron amplitude β_x in blue and the octupole strength k_3 in yellow for the nonlinear lens.

The results of the simulations are compared against the exact analytic model, calculated only using the octupole coefficients from Eq. 12, is shown in Fig. 10. The truncated analytic model appears to give good agreement with the envelope of the centroid oscillations, especially for smaller emittances where the decoherence is weaker. For very rapid decay of oscillation amplitude in the 16 mm-mrad case the analytic result seems to overestimate the decoherence strength. The disagreement is likely due to the area of validity of Eq. 3 and to the increasing importance of higher order terms at larger amplitudes.

VI.   CONCLUSION

A procedure for maintaining partial integrability for an elliptical potential, nonlinear element installed in the IOTA ring has been demonstrated. This will allow for suppression of collective instabilities even in the presence of space charge. The verification of this process and a demonstration of nonlinear decoherence in the presence of space charge has also been shown in simulations of IOTA. From this it can be seen that the nonlinear decoherence strength provided by the nonlinear element depends strongly on beam emittance. This dependence has been empirically qualified from simulation data. A simple analytic model also is has been shown that provides some insight into the emittance dependence, though it is limited to the cases where space charge may be neglected.

It is expected that future work will look to expand this analytic model to better capture inclusion of space charge in producing tune spread in the bunch that must be accounted for. Higher order terms could also be included, past the octupole. The current analytic model

may also be appropriate to apply to planned electron experiments in IOTA and could provide insight into nonlinear decoherence behavior in this case where space charge is negligible.
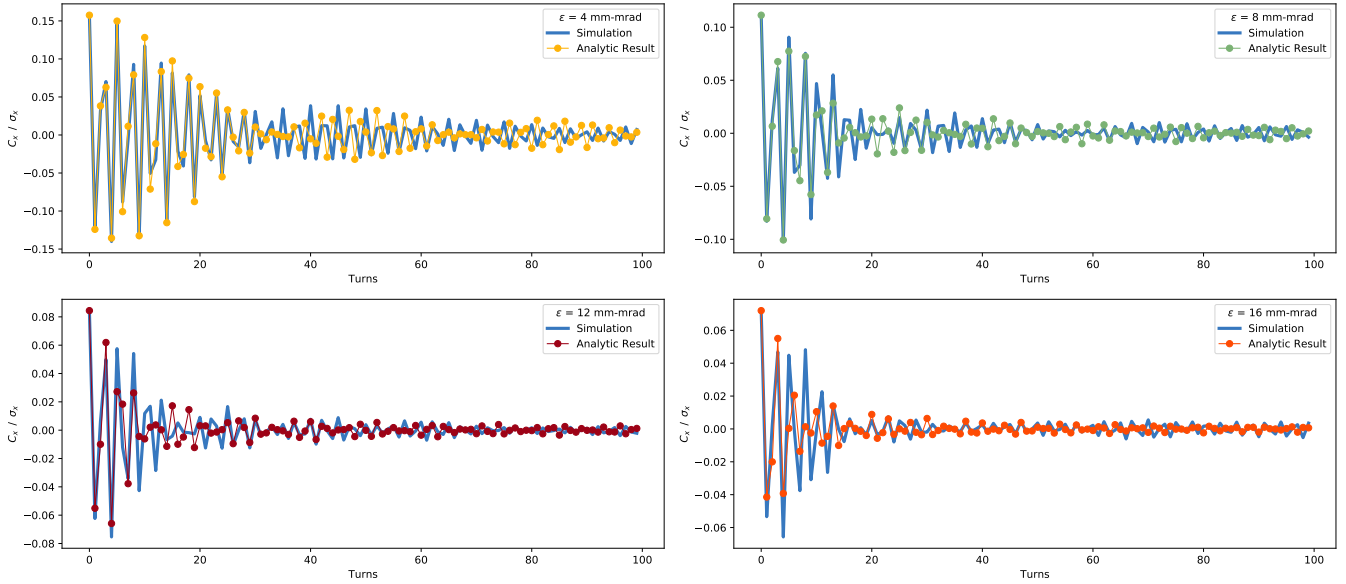
FIG. 10: Comparison of the analytic decoherence model to Synergia simulations of IOTA. The comparison is performed for bunches with four different emittances. From left to right and top to bottom $\varepsilon = 4, 8, 12, 16$ mm-mrad are shown.

[1] S. Peggs *et al.*, *ESS Technical Design Report*, Tech. Rep. (European Spallation Source, 2013).

[2] V. Lebedev *et al.*, *"PIP-II Reference Design Report"*, Tech. Rep. PIP-II DocDb 1 (FNAL, 2015).

[3] J. O'Connell, T. Wangler, R. Mills, and K. Crandall, in *Proc. of Part. Accel. Conf.* (1993) p. 3657.

[4] R. L. Gluckstern, Phys. Rev. Lett. **73**, 1247 (1994).

[5] R. Jameson, *Self-Consistent Beam Halo Studies & Halo Diagnostic Development in a Continuous Linear Focusing Channel*, Tech. Rep. LA-UR-94-3753 (Los Alamos National Laboratory, 1994).

[6] D. L. Bruhwiler, in *AIP Conf. Proc.*, Vol. 377 (1995) pp. 219–233.

[7] E. D. Courant and A. M. Sessler, Rev. Sci. Instr. **37** (1966).

[8] E. Ferlenghi, C. Pellegrini, and B. Touschek, Nuovo Cimento **44**, 253 (1966).

[9] R. Talman, Nucl. Instrum. Methods **193**, 423 (1982).

[10] C. Pellegrini, Nuovo Cimento **64A**, 447 (1969).

[11] V. Danilov and S. Nagaitsev, Phys. Rev. ST – Acc. Beams **13** (2010).

[12] S. Nagaitsev, A. Valishev, and V. Danilov, in *Proceedings of HB2010*, THO1D01 (2010).

[13] S. D. Webb, D. L. Bruhwiler, D. T. Abell, A. Shishlo, V. Danilov, S. Nagaitsev, A. Valishev, K. Danilov, and J. R. Cary, "Effects of nonlinear decoherence on halo formation," (2012), arXiv:1205:7083.

[14] S. Antipov, D. Broemmelsiek, D. Bruhwiler, D. Edstrom, E. Harms, V. Lebedev, J. Leibfritz, S. Nagaitsev, C. Park, H. Piekarz, P. Piot, E. Prebys, A. Romanov, J. Ruan, T. Sen, G. Stancari, C. Thangaraj, R. Thurman-Keup, A. Valishev, and V. Shiltsev, Journal of Instrumentation **12**, T03002 (2017).

[15] S. Webb, D. Bruhwiler, V. Danilov, R. Kishek, S. Nagaitsev, and A. Valishev, in *Proceedings, 6th International Particle Accelerator Conference (IPAC 2015): Richmond, Virginia, USA, May 3-8, 2015* (2015) p. MOPMA029.

[16] "Synergia simulation package," https://cdcvs.fnal.gov/redmine/projects/synergia2.

[17] F. OShea, R. Agustsson, A. Murokh, and E. Spranza, .

[18] A. Romanov, A. Valishev, D. Bruhwiler, N. Cook., and C. Hall, in *Proceedings of NAPAC2016*, THPOA23 (2016).

[19] R. E. Meller, A. W. Chao, J. M. Peterson, S. G. Peggs, and M. Furman, Tech. Rep. SSC-N-360 (Superconducting Super Collider, 1987).

[20] S. G. Peggs and R. M. Talman, Ann. Rev. Nucl. Part. Sci. **36**, 287 (1986).